Green Energy and Resources 2 (2024) 100058

Contents lists available at ScienceDirect

Green Energy and Resources

journal homepage: www.journals.elsevier.com/green-energy-and-resources

Research Article

High performance all-solid-state Li–Se battery based on selenium loaded on Ti_3C_2 MXene cathode

Renbo Liu [a,1], Chongxing Li [a,1], Qingyu Li [a,1], Shuxian Zhang [a], Chengxiang Wang [a], Zhiwei Zhang [a,**], Yuanchang Shi [a,***], Lidong Yang [b], Longwei Yin [a], Rutao Wang [a,*]

[a] Key Laboratory for Liquid-Solid Structural Evolution and Processing of Materials, Ministry of Education, School of Materials Science and Engineering, Shandong University, Ji'nan 250061, China

[b] Department of Industrial and Systems Engineering, The Hong Kong Polytechnic University, Hong Kong SAR 999077, China

ARTICLE INFO

Keywords:
Li–Se batteries
Solid-state electrolyte
Lithium argyrodite
MXene
Composite

ABSTRACT

Selenium has high theoretical volumetric capacity of 3253 mAh cm^{-3} and acceptable electronic conductivity of 1×10^{-5} S m^{-1}, which is considered as a potential alternative to sulfur cathode for all-solid-state rechargeable batteries with high energy density. However, the development of all-solid-state Li–Se batteries (ASSLSBs) are hindered by sluggish kinetics and poor cycling life. In this work, trigonal Se nanocrystallines are homogenously distributed in the interspace and on the surface of MXene layers (denoted as Se@MXene composite) by a novel melt-diffusion method. ASSLSBs based on this Se@MXene composite cathode exhibit large specific capacity of 632 mAh g^{-1} at 0.05 A g^{-1}, high-rate capability over 4 A g^{-1}, and excellent cycling stability over 300 cycles at 1 A g^{-1}. The ex-situ analytical techniques demonstrate that the excellent electrochemical performance of Se@MXene cathode largely arises from structural stability with the assistance of conductive MXene and reversible redox behavior between Li_2Se and Se during the repeating charge/discharge process. Our study points out the potential of material design of Se cathode based on conducting 2D materials with good electrochemical behavior, which may accelerate the practicability of ASSLSBs.

1. Introduction

Li–Se batteries operate with the conversion reactions between Se and Li_2Se to storage charge, exhibiting a large theoretical volumetric energy density over 3253 mAh cm^{-3} which overcome the energy limitations of insertion-oxide cathode and graphite anodes in lithium-ion batteries (LIBs) (Abouimrane et al., 2012; Dong et al., 2021; Wang et al., 2023; Mamoor et al., 2023). Up to now, many classical Li–Se batteries based on liquid electrolytes have been exploited, however, suffering from several safe issues including leakage, flammability and instability primarily caused by liquid electrolytes (Xu et al., 2019; Guo et al., 2022). Besides, during the charge/discharge process, intermediate products-polyselenides ((Li_2Se_n, $n > 4$)) will be formed in liquid electrolytes, which is soluble in nature, thus leading to intractable "shuttle effect" (Eftekhari et al., 2017; Li et al., 2022). Moreover, Li–Se batteries usually employed metal Li as the anode directly, hence the growth of Li dendrites in the liquid electrolytes is inevitable (Piao et al., 2023). Hence, the introduction of inflammable solid-state electrolytes (SSEs) into Li–Se batteries to replace the liquid electrolytes is considered as a promising approach to address the issues in liquid Li–Se batteries (Li et al., 2024).

Currently, various organic SSEs, such as $Li_{5.5}PS_{4.5}Cl_{1.5}$ (Lin et al., 2022), $Li_{1.5}Al_{0.5}Ge_{1.5}(PO_4)_3$ (Zhou et al., 2017), Li_3PS_4(Li et al., 2018), $Li_{10}GeP_2S_{12}$(Zhang et al., 2020a), and Li_3ErBr_6(Shi et al., 2023), had been extensively employed to fabricate ASSLSBs. In these ASSLSBs, Se can be electrochemically reduced to Li_2Se through one-step redox reaction, which potentially solve the "shuttle effect" caused by polyselenide during the lithiation process. Besides, the safety concerns from leakage and combustion of liquid electrolytes as well as the lithium dendrite growth, to some extent, can be alleviated by SSEs(Zhang et al., 2023). However, the stiffness of SSEs leads to the large stress/strain and interfacial resistance. In addition, the redox reaction between Se and Li_2Se brings out the large volume change (>98%), thus leading to the poor rate

* Corresponding author.
** Corresponding author.
*** Corresponding author.
E-mail addresses: zhangzhiwei@sdu.edu.cn (Z. Zhang), yuanchangshi@sdu.edu.cn (Y. Shi), Rtwang@sdu.edu.cn (R. Wang).
[1] These authors contributed equally to this work.

https://doi.org/10.1016/j.gerr.2024.100058
Received 14 November 2023; Received in revised form 20 February 2024; Accepted 23 February 2024

and short cycle life of ASSLSBs(Zhang et al., 2020a). Until now, many novel strategies have been explored to solve the above issues through using a porous conducing host-typically composed of porous carbon. However, recent studies found that Se would detach from porous carbon and agglomerate into Se particles or strips after the long-term cycles (Guo et al., 2022; Li et al., 2023), which leads to the low utilization of Se and short cycling life of ASSLSBs. Such enrichment of Se arouses the concern of incompatibility between Se and carbon substrate. The primary reason is that the ionic transport in carbon matrix is rather sluggish, then the redox reaction of Se may not conduct fully in the pores of carbon matrix. Therefore, host materials for Se in ASSLSBs should have the properties in highly conductive in ions and electrons as well as strong interactions with Se.

Two-dimensional transition metal carbides (MXenes) are promising candidates because of their high electrical conductivity, functionalized surfaces, large surface area, high mechanical strength and good flexibility (Xiao et al., 2019; Cao et al., 2020). Most importantly, MXenes have been demonstrated to be an ideal mixed ionic−electronic dual-carrier conducting framework (Oh et al., 2023). In this work, Ti_3C_2-MXene is employed to as the substrate to load Se nanoparticles through a novel melt diffusion method. As-achieved Se@MXene composite cathode displays a large reversible capacity of 632 mAh g^{-1} at 50 mA g^{-1}, a reversible capacity of 274 mAh g^{-1} at a high rate of 4000 mA g^{-1}, and a long-term cycle life. Ex-situ Raman and XPS analysis uncover that the good Li^+ charge storage of Se@MXene cathode arises from high reversibility of redox reaction between Li_2Se and Se as well as structural stability with the help of the conductive MXene substrate (Luo et al., 2023).

2. Material and methods

2.1. Materials synthesis

Exfoliation of Ti_3AlC_2 was achieved by a common HF etching method. Typically, 2 g of Ti_3AlC_2 powder purchased from Laizhou Kaixitaochicailiao Ltd. was firstly added into 20 ml of HF solution with a concertation of 40 wt% (Sinopharm Chemical Reagent) and stirred at room temperature for 24 h to etch the Al atoms. The deionized water was added into the above mixture. Then the Ti_3C_2 MXene precipitate can be achieved by centrifugation. The precipitate was washed with water and centrifugation for several times until the pH value of the precipitate is larger than 6. Then the precipitate was dried in a freeze dryer for 24 h to obtain the Ti_3C_2 MXene powder. To further remove the residual water, Ti_3C_2 MXene powder was heated in the oven for more than 24 h at 60°C and then transferred into glovebox.

Se@MXene composite was firstly prepared by grinding selenium powder with Ti_3C_2 MXene in a mortar and pestle with a mass ratio of 1.5:1 for 30 min. After that, the mixture obtained in the previous step was sealed in a glass tube. The sealed glass tube was then heated in a muffle furnace (Heifei MTI, KSL-1100X–S) at 300°C for 12 h. The heating rate is set to 5°C min^{-1}. The final Se@MXene composite was obtained after the temperature of muffle furnace is naturally down to room temperature.

The synthesis of $Li_{5.5}PS_{4.5}Cl_{1.5}$ electrolyte includes two steps of high-energy ball milling and annealing treatment. Li_2S (Macklin, 99.9%), P_2S_5 (Macklin, 99%), and LiCl (Aladdin, 99%) with stoichiometric ratio were milled at 300 rpm for 10 h using a ball mill (Changsha MITR, YXQM-1L) followed by sintering at 530°C for 10 h in a quartz tube.

2.2. Structural characterization

The morphology of as-prepared Ti_3C_2 MXene and Se@MXene samples was studied by Field emission scanning electron microscopy (FESEM, SU-70, Hitachi, Japan). The structure of as-prepared Ti_3C_2 MXene and Se@MXene samples was investigated by transmission electron microscopy (TEM, Tecnai F20). Powder X-ray diffraction (XRD, Rigaku D/Max-2400, Japan) using Cu-Ka radiation was employed to probe the structure and composition of Ti_3C_2 MXene and Se@MXene samples. Raman spectra of samples was achieved by a micro-Raman spectroscope (JY-HR800, excitation wavelength of 532 nm). The surface structure and functionalities of samples were recorded by X-ray photoelectron spectroscopy (XPS, PerkinElmer PHI-5702 Spectrometer). The pore structure and surface area of samples were studied by an ASAP 2020 volumetric adsorption analyzer (Micromeritics, USA) at 77 K. Thermogravimetric analysis (TGA, PerkinElmer, DSC8000, USA) was conducted under N_2. The heating rate is controlled to 10°C min^{-1} during TGA test.

2.3. Fabrication of cell

Briefly, the cathodes were prepared by milling 45 wt% of active materials (Se@MXene), 5 wt% of VGCF, and 50 wt% of $Li_{5.5}PS_{4.5}Cl_{1.5}$ in a planetary ball mill with a rotate speed of 600 rpm for 1 h (Changsha MITR, YXQM-1L) using ZrO_2 containers and balls. The Se cathodes were prepared in a similar way. 45 wt% of Se powder (After drying at 300°C for 12 h), 5 wt% of VGCF, and 50 wt% of $Li_{5.5}PS_{4.5}Cl_{1.5}$ were ball-milled together for 1 h at 600 rpm. Laboratory-scale ASSLSBs (Se@MXene or bare Se/$Li_{5.5}PS_{4.5}Cl_{1.5}$/Li–In) were assembled. The cathode power (upper layer) and $Li_{5.5}PS_{4.5}Cl_{1.5}$ powder (bottom layer) were pressed together into a two-layer pellet (12.7 mm in diameter) by cold pressing with a pressure of ~300 MPa. A Li–In disc was then attached on the electrolyte side of pellet to achieve a three-layer pellet. The three-layer pellet was then put into a commercial pressure die under a pressure of 50 MPa, which was sandwiched between two stainless steel rods (worked as current collectors).

2.4. Electrochemical measurements

Galvanostatic charge/discharge (GCD) measurements and life-span test of our ASSLSBs cell were performed on a Land CT2001A battery test system (Wuhan Land Electronics, Ltd., China). Cyclic voltammetry (CV) test and electrical impedance spectroscopy (EIS) test were recorded by a CHI760E (Shanghai Chenghua Electronics, Ltd., China). The working potential range of ASSLSBs is set to 0.4–2.4 V (vs Li^+/Li–In). The specific capacity values of our ASSLSBs were calculated by the active mass loading of Se.

3. Result and discussion

Fig. 1a schematically depicts the preparation process of Se@MXene. Typically, Ti_3C_2 MXene with an accordion-like layered structure was achieved by selectively etching Al element based intermediate layer of Ti_3AlC_2 (Fig. S1) (Luo et al., 2017). Then, MXene and Se powder were well mixed in a mortar and then head at 300°C. The heating temperature is higher than the melting point temperature of Se (217°C), then leading to melted Se. The melted Se would diffuse into the interlayer structure of MXene to form Se@MXene composite. The FESEM image in Fig. 1b show that as-prepared MXene is an accordion-like multilayer structure. Such accordion-like multilayer stacking structure provides space for accommodating Se nanoparticles. FESEM images in Fig. 1c and d displays that Se nanoparticles were dispersed on the surface and in the interspace of MXene layers. The average size of Se nanoparticles is evaluated to ~61 nm. Energy dispersive spectroscopy (EDS) mapping images in Fig. 1e–h shows Se nanoparticles are homogenously distributed in the whole MXene. High-resolution TEM (HRTEM) images of Se@MXene in Fig. 1i–k shows trigonal Se nanocrystallines were coated on the surface and infused into the stacking space of Ti_3C_2 MXenes sheets. The uniform distribution of Se on MXene is also confirmed by EDS mapping from TEM characterization (Fig. S2).

The XRD patterns of commercial Se, MAX, MXene and Se@MXene are summarized in Fig. 2a. The diffraction peaks corresponding to (002), (004) and (006) crystal planes can be found in the XRD spectra of MXene, indicating that HF successfully etched the MAX phase. Commercial Se shows several prominent peaks around 23.51°, 29.70°, 41.32°, 43.65°and 45.36°, corresponding to (100), (101), (110), (012) and (111) of trigonal Se (JCPDS no. 73~0465). After selenium is infused into

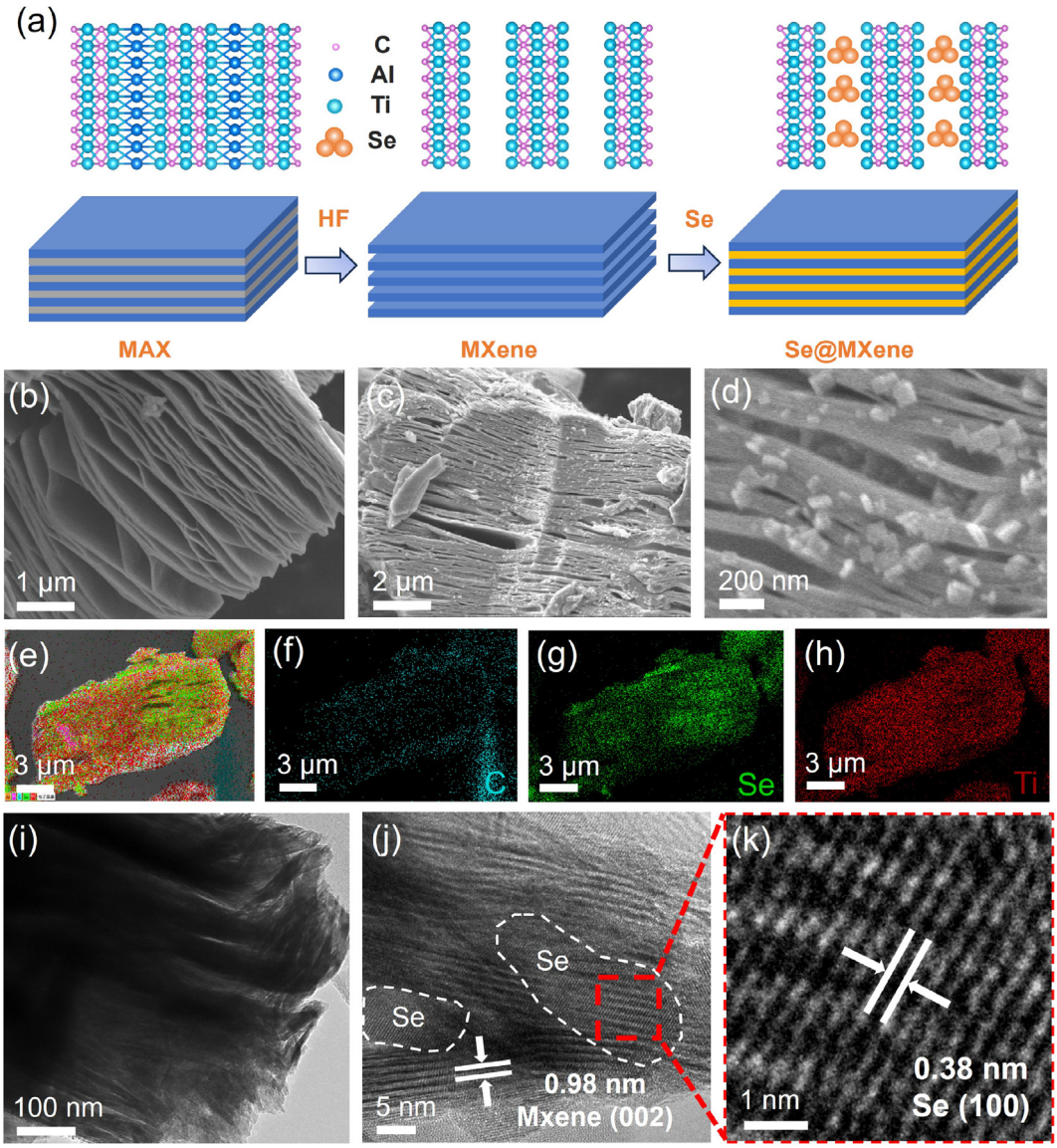

Fig. 1. (a) Schematic diagram of synthetic procedures for Se@MXene sample; SEM images of (b) MXene; (c), (d) Se@MXene; (e)–(h) EDS mapping of Se@MXene; (i) TEM images of MXene and (j) and (k) HRTEM images of Se@MXene.

MXene, the diffraction peaks of trigonal Se are detected. The average size of Se nanocrystallines loading on MXene is evaluated to ~19 nm through the Scherrer equation. Fig. 2b shows the Raman spectra of the trigonal Se, MXene and Se@MXene. Multiple peaks around 122 cm^{-1}, 207 cm^{-1}, 364 cm^{-1}, 621 cm^{-1}, and 714 cm^{-1}assigned to MXene were found (Sarycheva et al., 2020). Raman spectra of Se@MXene shows a strong peak at 236 cm^{-1} assigned to trigonal Se and several weak peaks (as stated above) assigned to MXene.

The full-scale XPS spectrum in Fig. 2c shows that MXene mainly contains C, F, Ti and O elements. For full-scale XPS spectrum of Se@MXene, besides the peaks contributed from MXene, additional peaks around 137.8, 161.7 and 178.7 eV assigned to Se elements were found. After loading selenium, the content of F element in the MXene sample decreased, while the content of O element increased. These changes in O and F contents are mainly caused by the substitution of the F-containing functional group and the partial oxidation of MXene. Fig. 2d displays the high-resolution spectra of C1s of MXenes and Se@MXene which can be deconvoluted into C–Ti (280.0 eV), C–C (284.6 eV) and C–O (285.1 eV) bonds. The C–F bonds at high binding energies around 289.0 eV were replaced by C–Se bonds around 287.8 eV after Se infusion (Liu et al., 2016). The high-resolution XPS spectra of Ti2p of MXene in Fig. 2e can be deconvoluted into six peaks, which can be assigned to Ti–C bonds (455.0 eV and 460.8 eV), Ti^{2+} bonds (455.9 eV for Ti^{2+} 2p3/2 and 461.7 eV for Ti^{2+} 2p1/2), Ti^{3+} bonds (457.0 eV for Ti^{3+} 2p3/2 and 462.9 eV for Ti^{3+} 2p1/2), and Ti^{4+} bonds (458.5 eV for Ti^{4+} 2p3/2 and 463.9 eV for Ti^{4+} 2p1/2) (Zhang et al., 2020). By contrast, an increase in peak intensities for Ti^{4+} bonds in Se@MXene may be associated to the partial oxidation of MXene during the annealing process. Fig. 2f shows the Se 3d XPS spectra which can be deconvoluted into three bonds of Se 3d5/2 (55.1 eV), Se 3d3/2 (55.9 eV), and Se–O/Se–C (59.8 eV). The formation of Se–C or Se–O bonds mainly results from the reaction between Se and O or C from MXene during the Se-diffusion process.

Fig. S3a shows that the nitrogen adsorption/desorption curve of MXene displays type H3 isotherms, indicating the slitlike pores formed on MXene caused by aggregates (loose assemblages) of platelike particles. MXene sample has the calculated BET surface area and pore volume of 3.39 $m^2\ g^{-1}$ and 0.016 $cm^3\ g^{-1}$, respectively. Fig. S3b shows MXene has the wide pore-size distribution ranging from 20 to 100 nm. After the incorporation of Se, Se@MXene still maintain type H3 isotherms with the apparently reduced adsorption volume. The BET surface area and pore volume of Se@MXene are decreased to 0.95 $m^2\ g^{-1}$ and 0.0048 $cm^3\ g^{-1}$, respectively, which suggest that Se was infused into the slitlike pores of

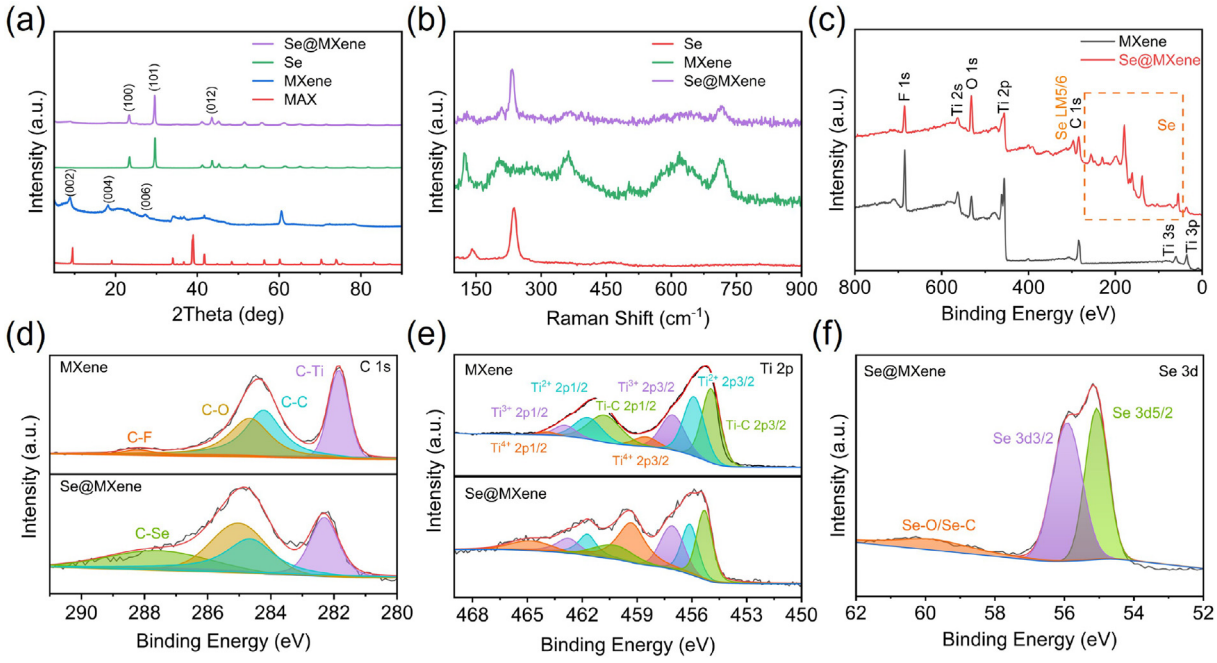

Fig. 2. (a) XRD patterns and (b) Raman spectra of Se, MXene and Se@MXene samples; (c) Survey; (d) C1s; (e) Ti 2p and (f) Se 3d XPS spectra of MXene and Se@MXene.

MXenes. The mass loading of Se in Se@MXene is evaluated to 63.3 wt% by TGA curves in Fig. S4. As a result, the above structural and spectral characterizations show that conductive MXene with the accordion-like multilayer provides many spaces to accommodate trigonal Se nanocrystallines, which may potentially enhance the overall electrochemical performance of Se (Yang et al., 2023).

To investigate the electrochemical performance of Se@MXene sample, a prototype ASSLSB was assembled by coupling the Se@MXene cathode, $Li_{5.5}PS_{4.5}Cl_{1.5}$ SSE, and Li–In anode. Fig. 3a depicts the cyclic voltammetry curves (CVs) of ASSLSBs at a sweep rate of 0.2 mV s^{-1}. The cathodic peak around 1.2 V (vs. In–Li) is mainly associated to the reduction reaction of Se to Li_2Se ($Se + 2Li^+ + 2\,e^- \rightarrow Li_2Se$) (Schwietert et al., 2020). For the anodic process, only one peak around 1.8 V (vs. In–Li) appears, which is associated to oxidation reaction of Li_2Se to Se. From the second cycle to the fifth cycle, these CV curves tend to overlapping, suggesting the good electrochemical reversibility of Se@MXene.

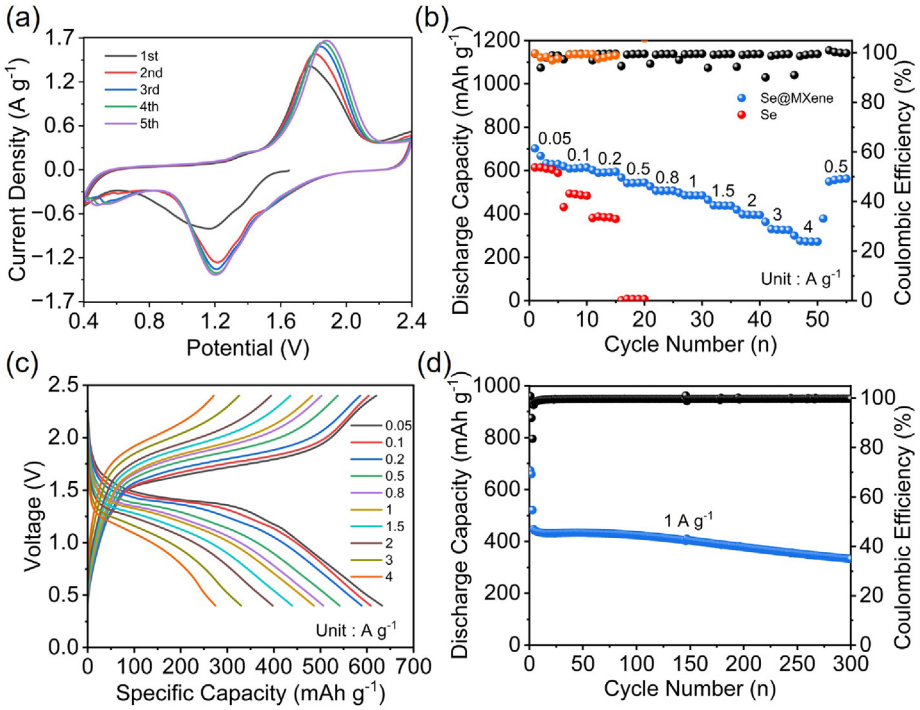

Fig. 3. Electrochemistry behavior of Se@MXene cathode in solid-state battery with an operating potential of 0.4~2.4 V (vs Li–In/Li^+). (a) CVs curves at 0.2 mV s^{-1}; (b) Specific capacities of Se@MXene cathode and Se cathode under the different discharging current densities; (c) Typical charging/discharging curves under the different rates; (d) Cycling performance at 1 A g^{-1} (50 mA g^{-1} for initial 2 cycles).

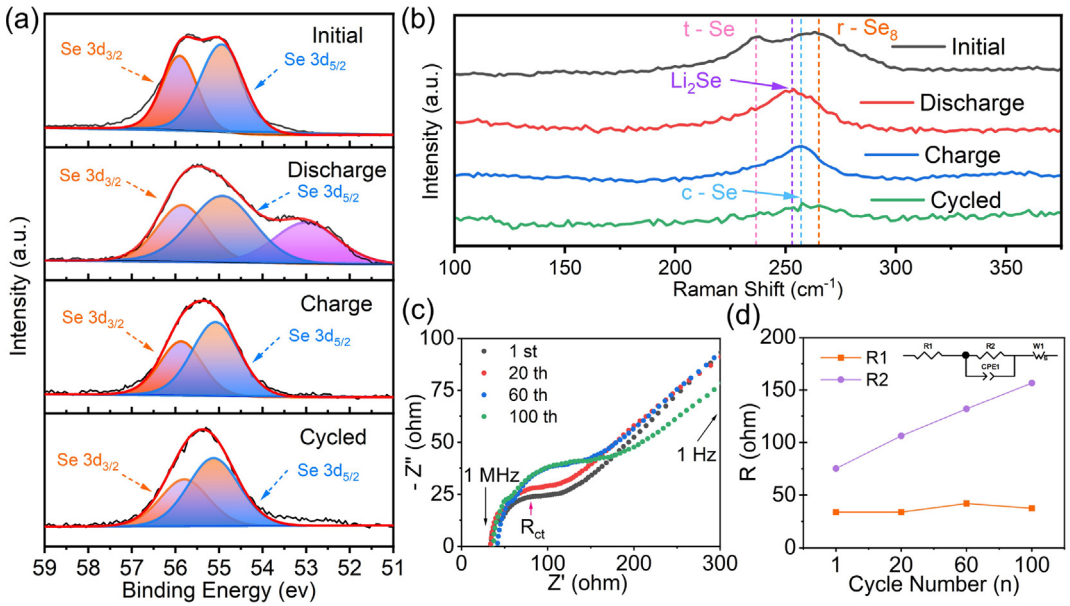

Fig. 4. (a) XPS spectra of different charge/discharge states of Se@MXene cathode; (b) Raman spectra of different charge/discharge states of Se@MXene cathode; (c) Nyquist plots of Se@MXene cathode during long-term cycles; (d) Evolution of impedance with different cycles. The inset figure in (d) is the equivalent circuit for EIS fitting.

Fig. 3b plots the typical GCD curves under the different rates. The specific capacities of Se@MXene could be evaluated to 632, 608, 540, 485, 397, and 274 mAh g^{-1} at the rates of 0.05, 0.1, 0.5, 1.0, 2.0 and 4.0 A g^{-1}, respectively, suggesting the excellent rate capability. In contrast, the specific capacity of bare MXene-enabled Li–Se batteries could be evaluated to 614, 493, 387 and 8 mAh g^{-1} at the current densities of 50, 100, 200 and 500 mA g^{-1}, which is apparently inferior to that of Se@MXene cathode based ASSLSBs. The GCD curves shown in Fig. 3c exhibit one predominant plateau around 1.5 V, corresponding to redox couple of CVs in Fig. 3a. To investigate redox reaction kinetics of Se@MXene, galvanostatic intermittent titration technique (GITT) at 0.1 A g^{-1} was carried out to evaluate the diffusion coefficient Li^+ (D_{Li}) in the Se@MXene electrode (Fig. S5). As shown in Fig. S5, only one plateau can be observed after full relaxation, which indicates a one-step solid–solid phase transition between Se and Li_2Se during the discharge/charge process. The D_{Li} value can be calculated by solving Fick' second law based on the GITT potential curves. During the discharge process, the D_{Li} value shows a sharp decrease in the initial process, and then rises slowly before remaining basically stable. The D_{Li} value during the charging process is same as that of the discharging process. The D_{Li} values for Se@MXene cathode fall in between 6.97×10^{-12} and 3.21×10^{-16} cm^2 s^{-1}, suggesting the fast Li^+ diffusion in Se@MXene electrode.

Moreover, the Se@MXene cathode shows the excellent cycling stability. Se@MXene cathode achieves a capacity retention value of 97% after 100 cycles at 0.2 A g^{-1} (Fig. S6). Even after the constant 300 cycles under 1.0 A g^{-1}, Se@MXene cathode achieves a capacity retention value of 74% (Fig. 3d). The coulombic efficiency values are approximately 100% during the whole cycling test. Besides, the profile of charge/discharge curves during the whole cycling shows one predominant plateau without no apparent change (Fig. S7).

Ex-situ XPS and Raman measurements were further carried out to probe the redox mechanism of Se@MXene cathode in ASSLSB. Fig. 4a depicts that the Se 3d XPS spectra of Se@MXene cathode can be deconvoluted into Se 3d 5/2 (54.9 eV) and Se 3d3/2 (55.9 eV) peaks. After the initial discharge, besides the main peaks of Se 3d, a new peak around 53 eV is found, apparently relating to the formation of Li_2Se(Guo et al., 2022; Li et al., 2023; Park et al., 2021). After the initial charge process and the followed long cycles, the peak around 53 eV disappears and the profile of Se 3d spectra shows no apparent change compared to pristine state, suggesting the reversible redox behavior of Se in Se@MXene cathode. Fig. 4b shows the ex-situ Raman spectra of pristine Se@MXene electrode. Raman spectra suggests that Se in Se@MXene is mainly composed by trigonal Se (t-Se) and Se_8 rings (r-Se_8), as indicated by Raman shift at 236.6 cm^{-1} and 265.1 cm^{-1}, respectively. Se_8 rings probably originates from the partial structural transformation from trigonal Se during the thermal infusion process, which are usually observed for Se loading on porous substrates (Yang et al., 2013). After the initial discharge to 0.4 V, pristine Se is transformed into Li_2Se as suggested by the Raman shift of the product at 253 cm^{-1}. When charged back to 2.4 V, Li_2Se is transformed into chain-like Se (c-Se) instead of trigonal Se and Se_8 rings as suggested by the Raman shift of the product at 257 cm^{-1} (Yang et al., 2013). c-Se products still predominate even after the long cycles. As we know, the binding between c-Se and MXene is stronger than that of r-Se_8, thus the Se detaching from MXene may happen with a low frequency (Li et al., 2023; Yang et al., 2013). As expected, Se atoms in the Se@MXene cathode are homogenous distribution before and after the cycling (Figs. S8–S12), which is different from Se-carbon composites in which uneven Se strips or particles appear after the cycling (Guo et al., 2022; Li et al., 2023). This is probably the main reason for ASSLSB based on Se@MXene cathode has the excellent electrochemical performance. We further employed EIS spectra to uncover the degradation mechanism of this ASSLSB based on Se@MXene during the (de)lithiation process (Fig. 4c). The corresponding Nyquist plots were fitted with the equivalent circuit (R1 (R2Q1)Q2) shown in Fig. 4d, where R1 represents the internal resistance from the cell and electrode materials, R2Q1 (or R_{ct}Q1) represent interfacial charge transfer, and Q2 represents Li^+ diffusion process in bulk. The R2 values increase gradually during the long-term cycling, suggesting unstable interfaces of SE|Se@MXene caused by the repeated volume changes between Se and Li_2Se, then leading to the decay in capacity during the cycles.

4. Conclusion

In conclusion, we successfully demonstrated feasible ASSLSBs based on the Se@MXene composite cathode. The Se@MXene composite was achieved by a facile melt diffusion route. Trigonal Se nanocrystallines with a mass loading of 63.3 wt% are distributed on the surface and in the interspace of layers of conductive MXene. The Se@MXene cathode

displays a large specific capacity of 632 mAh g^{-1} (93.6% of theoretical capacity) at 50 mA g^{-1} and still deliver a reversible capacity of 274 mAh g^{-1} at a high rate of 4000 mA g^{-1}. In addition, The Se@MXene cathode was cycled stably over 300 cycles. We find that the irreversible conversion of t-Se and r-Se_8 to Li_2Se and then to c-Se on the conductive MXene during the initial charge/discharge process and the reversible conversion between c-Se and Li_2Se during the followed process though ex-situ Raman and XPS spectra. With the unique advantages of Se@MXene composite in convenient synthetic method and enhanced electrochemical performance, this composite will work as the new cathode material for solid-state electrochemical energy storage devices.

Declaration of competing interest

The authors declare no competing financial interest.

Acknowledgements

This work was supported by the National Natural Science Foundation of China (52272224, 51902188), Innovation Capacity Improvement Project of Small and Medium-Sized Technology-Based Enterprise of Shandong Province (2021TSGC1149), and Youth Innovation Team Project of Shandong Provincial Education Department (10000082295015).

Appendix A. Supplementary data

Supplementary data to this article can be found online at https://doi.org/10.1016/j.gerr.2024.100058.

References

Abouimrane, A., Dambournet, D., Chapman, K.W., et al., 2012. A new class of lithium and sodium rechargeable batteries based on selenium and selenium-sulfur as a positive electrode. J. Am. Chem. Soc. 134, 4505–4508. https://doi.org/10.1021/ja211766q.

Cao, Z.J., Zhang, Y.Z., Cui, Y.L.S., et al., 2020. Harnessing the unique features of MXenes for sulfur cathodes. Tungsten-Singapore 2, 162–175. https://doi.org/10.1007/s42864-020-00047-5.

Dong, Y.F., Lu, P.F., Ding, Y.J., et al., 2021. Advanced design of cathodes and interlayers for high-performance lithium-selenium batteries. SusMat 1, 393–412. https://doi.org/10.1002/sus2.26.

Eftekhari, A., 2017. The rise of lithium-selenium batteries. Sustain. Energy Fuels 1, 14–29. https://doi.org/10.1039/c6se00094k.

Guo, B.Y., Wang, Z.F., Chen, J.Z., et al., 2022. Cryo-em revealing the origin of excessive capacity of the Se cathode in sulfide-based all-solid-state Li-Se batteries. ACS Nano 16, 17414–17423. https://doi.org/10.1021/acsnano.2c08558.

Li, X.N., Liang, J.W., Li, X., et al., 2018. High-performance all-solid-state Li-Se batteries induced by sulfide electrolytes. Energy Environ. Sci. 11, 2828–2832. https://doi.org/10.1039/c8ee01621f.

Li, X.N., Liang, J.W., Kim, J.T., et al., 2022. Highly stable halide-electrolyte-based all-solid-state Li-Se batteries. Adv. Mater. 34 8. https://doi.org/10.1002/adma.202200856.

Li, C.X., Liu, R.B., Zhang, S.X., et al., 2023. Advanced all-solid-state lithium-selenium batteries enabled by selenium-nitrogen doped hierarchic meso-microporous carbon nanospheres composite cathode. Chin. Chem. Lett. 34, 5. https://doi.org/10.1016/j.cclet.2022.108083.

Li, Q., Chen, J., Zhang, S., et al., 2024. The developments, challenges, and prospects of solid-state Li-Se batteries. Energy Storage Mater. 65. https://doi.org/10.1016/j.ensm.2023.103138.

Lin, J.Y., Chen, S., Li, J.Y., et al., 2022. Chlorine-rich lithium argyrodites enables superior performances for solid-state Li-Se batteries at wide temperature range. Rare Met. 41, 4065–4074. https://doi.org/10.1007/s12598-022-02093-z.

Liu, Y., Shen, Y.T., Sun, L.T., et al., 2016. Elemental superdoping of graphene and carbon nanotubes. Nat. Commun. 7 9. https://doi.org/10.1038/ncomms10921.

Luo, J.M., Zhang, W.K., Yuan, H.D., et al., 2017. Pillared structure design of mxene with ultralarge interlayer spacing for high-performance lithium-ion capacitors. ACS Nano 11, 2459–2469. https://doi.org/10.1021/acsnano.6b07668.

Luo, J., Qiu, S., Wang, H., et al., 2023. Rationally designed tungsten trioxide nanosheets for high-efficiency aqueous battery application. Green Energy Res. 1, 100008. https://doi.org/10.1016/j.gerr.2023.100008.

Mamoor, M., Li, Y., Wang, L., et al., 2023. Recent progress on advanced high energy electrode materials for sodium ion batteries. Green Energy Res. 1, 100033. https://doi.org/10.1016/j.gerr.2023.100033.

Oh, J., Choi, S.H., Kim, J.Y., et al., 2023. Anode-less all-solid-state batteries operating at room temperature and low pressure. Adv. Energy Mater. 9. https://doi.org/10.1002/aenm.202301508.

Park, H., Kim, J., Lee, D., et al., 2021. Epitaxial growth of nanostructured Li_2Se on lithium metal for all solid-state batteries. Adv. Sci. 8 7. https://doi.org/10.1002/advs.202004204.

Piao, Z.H., Gao, R.H., Liu, Y.Q., et al., 2023. A review on regulating Li^+ solvation structures in carbonate electrolytes for lithium metal batteries. Adv. Mater. 35 22. https://doi.org/10.1002/adma.202206009.

Sarycheva, A., Gogotsi, Y., 2020. Raman spectroscopy analysis of the structure and surface chemistry of $Ti_3C_2T_x$ MXene. Chem. Mater. 32, 3480–3488. https://doi.org/10.1021/acs.chemmater.0c00359.

Schwietert, T.K., Arszelewska, V.A., Wang, C., et al., 2020. Clarifying the relationship between redox activity and electrochemical stability in solid electrolytes. Nat. Mater. 19, 428. https://doi.org/10.1038/s41563-019-0576-0.

Shi, X.M., Zeng, Z.C., Zhang, H.T., et al., 2023. Encapsulating and operating a stable Li_3ErBr_6-based solid Li-SeS_2 battery at room temperature. Adv. Funct. Mater. 33 7. https://doi.org/10.1002/adfm.202213638.

Wang, W., 2023. Green energy and resources: advancing green and low-carbon development. Green Energy Res. 1, 10009. https://doi.org/10.1016/j.gerr.2023.100009.

Xiao, Z.B., Li, Z.L., Meng, X.P., et al., 2019. MXene-engineered lithium-sulfur batteries. J. Mater. Chem. A 7, 22730–22743. https://doi.org/10.1039/c9ta08600e.

Xu, G.-L., Sun, H., Luo, C., et al., 2019. Solid-state lithium/selenium–sulfur chemistry enabled via a robust solid-electrolyte interphase. Adv. Energy Mater. 9, 1802235. https://doi.org/10.1002/aenm.201802235.

Yang, C.P., Xin, S., Yin, Y.X., et al., 2013. An advanced selenium-carbon cathode for rechargeable lithium-selenium batteries. Angew. Chem.-Int. Edit. 52, 8363–8367. https://doi.org/10.1002/anie.201303147.

Yang, K., Fan, Q., Song, C., et al., 2023. Enhanced functional properties of porous carbon materials as high-performance electrode materials for supercapacitors. Green Energy Res. 1, 100030. https://doi.org/10.1016/j.gerr.2023.100030.

Zhang, J.Z., Kong, N., Hegh, D., et al., 2020. Freezing titanium carbide aqueous dispersions for ultra-long-term storage. ACS Appl. Mater. Interfaces 12, 34032–34040. https://doi.org/10.1021/acsami.0c06728.

Zhang, Q., Cai, L.T., Liu, G.Z., et al., 2020a. Selenium-infused ordered mesoporous carbon for room-temperature all-solid-state lithium-selenium batteries with ultrastable cyclability. ACS Appl. Mater. Interfaces 12, 16541–16547. https://doi.org/10.1021/acsami.0c01996.

Zhang, S., Chen, J., Zhu, C., et al., 2023. Robust all-solid-state lithium metal batteries enabled by a composite lithium anode with improved bulk Li diffusion kinetics properties. ACS Nano 17, 24290–24298. https://doi.org/10.1021/acsnano.3c09853.

Zhou, Y.C., Li, Z.J., Lu, Y.C., 2017. A stable lithium-selenium interface via solid/liquid hybrid electrolytes: blocking polyselenides and suppressing lithium dendrite. Nano Energy 39, 554–561. https://doi.org/10.1016/j.nanoen.2017.07.038.